Int J Fract (2007) 148:155–167
DOI 10.1007/s10704-008-9190-x

ORIGINAL PAPER

A fatigue crack initiation model incorporating discrete dislocation plasticity and surface roughness

Steffen Brinckmann · Erik Van der Giessen

Received: 15 April 2007 / Accepted: 23 February 2008 / Published online: 26 March 2008

Abstract Although a thorough understanding of fatigue crack initiation is lacking, experiments have shown that the evolution of distinct dislocation distributions and surface roughness are key ingredients. In the present study we introduce a computational framework that ties together dislocation dynamics, the fields due to crystallographic surface steps and cohesive surfaces to model near-atomic separation leading to fracture. Cyclic tension–compression simulations are carried out where a single plastically deforming grain at a free surface is surrounded by elastic material. While initially, the cycle-by-cycle maximum cohesive opening increases slowly, the growth rate at some instant increases rapidly, leading to fatigue crack initiation at the free surface and subsequent growth into the crystal. This study also sheds light on random local microstructural events which lead to premature fatigue crack initiation.

Keywords Dislocation · Cohesive surface · Surface roughness · Fatigue initiation

S. Brinckmann · E. Van der Giessen
Zernike Institute for Advanced Materials, University of Groningen, Groningen, The Netherlands

S. Brinckmann (✉)
Department of Material Science, California Institute of Technology, MC 308-81, Pasadena, CA 91125-8100, USA
e-mail: Steffen@caltech.edu

1 Introduction

Even though fatigue can be considered a long-standing problem, numerous experimental studies are being carried out even to date to explore fatigue crack initiation, predominantly in polycrystalline metals (e.g. Narasaiah and Ray 2008; Sackett et al. 2007; Polák 2007). While they have identified certain key building blocks of fatigue in fcc materials, their connection and interaction is not well understood. Mughrabi et al. (1979) and other researchers subsequently, have shown that during cyclic plastic deformation dislocations multiply and form structures in the bulk of the material. Brown and Ogin (1984) actually attribute crack initiation to the formation of a characteristic dislocation structure with a logarithmic singularity at the free surface. As the dislocations escape the material, they leave behind crystallographic surface steps (see, e.g., Vehoff 1994). Their accumulation leads to surface roughness which plays a vital role in crack initiation; repetitive removal of the roughness has been found to lead to a considerable increase in fatigue life (Hahn and Duquette 1978). On the other hand, Basinski and Basinski (1985) have observed fatigue in the absence of surface roughness.

Continuum models of fatigue crack initiation (e.g. Kratochvil 2001; Fine and Bhat 2007), by construction, cannot capture discrete microstructural events. Models that do include discrete crystalline events are, so far, mostly based on presumed dislocation structures (e.g. Antonopoulos et al. 1976; Essmann et al. 1981; Brown and Ogin 1984) or specific dislocation slip events

(e.g. Neumann 1969). Based on the work by Essmann et al. (1981), Repetto and Ortiz (1997) predicted the growth of a surface protrusion by employing a continuum model and attributed crack initiation to this evolution. One study where dislocation structures were not presumed but were the outcome of discrete dislocation simulations is that by Déprés et al. (2004) of a single ultra-fine grain with rigid grain-boundaries. In this study also the surface roughness has been determined, but the possibility of crack initiation was not included nor the dependence of the surface steps on the dislocation behavior. To the best of the authors' knowledge, no model is available at this moment that accounts for the evolution of the discrete surface roughness and of the dislocation distribution.

The present article introduces a computational framework that consists of three parts. The first, viz. the cohesive surface model of Xu and Needleman (1994), models the separation of atomic planes. The second part is an approximate elastic field due to the crystallographic surface roughness. Finally, a dislocation dynamics model represents plastic flow and incorporates the long-range elastic fields due to the dislocation distribution.

2 Model

2.1 Superposition

We model a sample of a plane strain specimen with an initially flat traction-free surface and the rest of its boundary subjected to either a prescribed displacement $\boldsymbol{u}_0$ or traction $\boldsymbol{t}_0$. As illustrated in Fig. 1a, inside this region the model accounts for (i) plastic deformation by the motion of discrete dislocations, (ii) the presence of cohesive surfaces and (iii) the development of surface roughness caused by dislocations exiting the material through the free surface. These three ingredients are discussed in more detail subsequently and are integrated by exploiting superposition.

The first ingredient of the approach, see Fig. 1b, is the two-dimensional dislocation dynamics model of Van der Giessen and Needleman (1995), as outlined in the following subsection. At each instant of time this part provides the $(\tilde{\ })$ fields due to the instantaneous distribution of dislocations.

The second part includes in an approximate way the modification of the fields in the neighbourhood of crystallographic surface steps. These correction fields, $(\bar{\ })$, are derived in Sect. 2.3 from the elastic solution of a wedge.

Finally, the cohesive surface and the boundary conditions are incorporated through the third part, sketched in Fig. 1d, whose solution is indicated by $(\hat{\ })$. A cohesive surface law is assumed with near-atomic properties which is reversible, i.e. we neglect oxidation and all other processes which alter the evolving crack surface and prevent it from healing.

Since each of the three fields pertain to a linear elastic material, we can use superposition to express the total stress and displacement fields as

$$\boldsymbol{\sigma} = \tilde{\boldsymbol{\sigma}} + \hat{\boldsymbol{\sigma}} + \bar{\boldsymbol{\sigma}}, \qquad \boldsymbol{u} = \tilde{\boldsymbol{u}} + \hat{\boldsymbol{u}} + \bar{\boldsymbol{u}}. \tag{1}$$

In Van der Giessen and Needleman (1995), the $(\hat{\ })$ fields correct the $(\tilde{\ })$ fields of the dislocation distribution for the boundary conditions; here, the $(\hat{\ })$ fields also correct for the $(\bar{\ })$ fields of the crystallographic surface steps. However, the non-surface boundaries S_{ext} are sufficiently far away that the $(\bar{\ })$ fields can be neglected in correcting for the prescribed displacements or tractions. Even though superposition can be applied inside the elastic solid, the third subproblem is nonlinear because of the cohesive law. As a consequence, the $(\hat{\ })$ solution is obtained in an incremental manner, as outlined in Sect. 2.4.

As mentioned before, we assume small strains, as in Van der Giessen and Needleman (1995). Recently, Deshpande et al. (2003) have introduced a finite strain formulation for discrete dislocation plasticity, but the combination with cohesive surfaces awaits implementation.

2.2 Dislocation dynamics

Subproblem (a) in Fig. 1 pertains to a semi-infinite, two-dimensional strip containing a single grain near its free surface in which plasticity takes place; neighboring grains in the polycrystalline material are assumed to be oriented such that no plastic flow takes place in them, see Fig. 2. The rectangular grain has three slip systems at 60° from each other (as a two-dimensional representation of an fcc crystal), one being favorably oriented for slip (the so-called primary slip system) at 45° from the remote tensile direction, which is parallel to the free surface.

Plastic flow inside the grain originates from the motion of discrete dislocations. Consistent with the

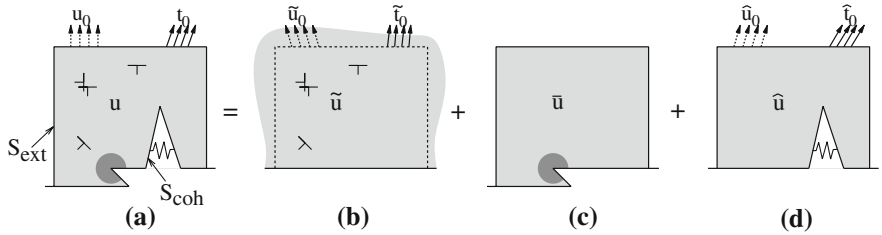

Fig. 1 The proposed framework (**a**) is a compilation of a dislocation model (**b**), a crystallographic surface step model (**c**) and a model to incorporate the cohesive surface and the boundary conditions (**d**)

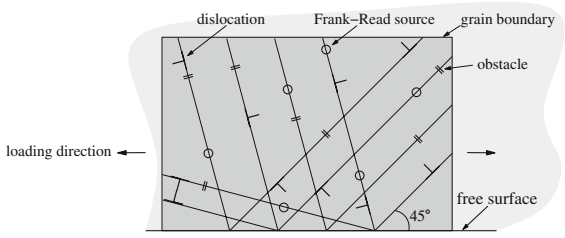

Fig. 2 Half-infinite strip of material with a single grain inside of which dislocation dynamics is applied; the surrounding material is elastic. The grain has three slip systems, one of which is oriented for maximal shear at 45° from the free surface

plane strain condition, all dislocations are of edge character with the Burgers vector in the plane of the model and of length b. They are treated as singularities in a linear elastic, isotropic continuum. Closed-form expressions are used for the long-range fields in the presence of a traction-free surface (Freund 1994), so that the free surface boundary condition is directly taken into account. From these singular stress fields and the contributions of the other parts of the framework, Eq. (1), along with the free surface image stress on the dislocation (Hirth and Lothe 1968), the Peach-Koehler force on each dislocation is calculated at each time step of the incremental calculation. This force governs the evolution of the dislocation structure through a number of constitutive rules.

Dislocation motion is confined to be by glide, with the velocity dependent on the Peach-Koehler force according to a linear drag relationship with a drag coefficient B. Climb or cross-slip are not modelled. The nucleation of new dislocations is incorporated through two-dimensional Frank-Read sources. These are randomly positioned and generate a dipole when the resolved shear stress exceeds the source strength τ_{nuc} for a sufficiently long time t_{nuc} (see Van der Giessen and Needleman (1995) for details). Dislocation annihilation occurs when the distance between two dislocations of opposite sign is less than a critical distance of $6b$. Furthermore, dislocations can escape from the grain at the free surface, leaving behind crystallographic surface steps. Finally, dislocations can get pinned at point obstacles. These either represent small precipitates or forest dislocations. If the Peach-Koehler force on the pinned dislocation exceeds the strength of the obstacle, $b\tau_{\text{obs}}$, the dislocation is released. Grain boundaries are assumed, for simplicity, to be impenetrable by dislocations.

The dislocation dynamics is simulated in an incremental fashion using straightforward Euler time integration. The time step employed, $\Delta t = 0.1$ ns, is small enough to capture events such as dislocation nucleation and junction formation. The dislocation structure that evolves is in no way presumed but is an outcome of the simulation, in which sources and obstacles are randomly distributed. With the constitutive rules outlined above, the uniaxial response of an isolated single grain is close to elastic-perfectly plastic.

2.3 Surface roughness

The surface roughness we include in the analysis is that produced by the accumulation of crystallographic surface steps that are left when dislocations leave the crystal. The interaction between surface steps is neglected, assuming that they are separated sufficiently well. Therefore, superposition of the fields of individual steps is used, so that the stress field $\bar{\boldsymbol{\sigma}}$ due to the surface roughness is given by

$$\bar{\boldsymbol{\sigma}} = \sum_{l} \bar{\boldsymbol{\sigma}}^{(l)} \tag{2}$$

where $\bar{\boldsymbol{\sigma}}^{(l)}$ is the stress due to an individual surface step l on a flat traction-free surface. The latter stress is defined to be the deviation from the uniform stress field when the strip is subjected to uniaxial tension parallel to the surface, Fig. 3.

Within the framework of linear elasticity adopted throughout this work, the stress field caused by each

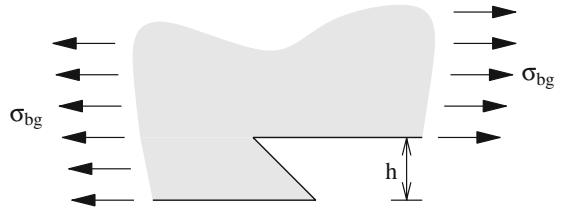

Fig. 3 A single crystallographic slip step of height h on a free surface caused by dislocations that have exited the crystal. The $\bar{\sigma}^{(l)}$ field in Eq. (2) is the local perturbation of the otherwise uniform uniaxial stress σ_{bg}

step is self-similar. Therefore, we determine the field for a representative surface step and scale all lengths by the step height h. The field is approximated by an asymptotic solution similar to that of a wedge, and, as detailed in the Appendix, can be written in the form

$$\bar{\sigma}^{(l)} = \sum_k r^{\lambda_k - 1} K_k \overset{*}{f}_k(\lambda_k, \theta), \tag{3}$$

$$K_k = a_k \sigma_{\mathrm{bg}} h^{1-\lambda_k}. \tag{4}$$

in polar coordinates (r, θ) from the tip of the wedge. $\overset{*}{f}$ is a non-dimensional tensor of closed-form expressions for the θ-dependence of the stresses. λ_k are non-dimensional eigenvalues, given in the Appendix, and a_k are non-dimensional scalars to fit the analytical expressions for the stress field to numerical results. The background stress is the sum of part (b) and (d) in Fig. 1 at the root of the surface step, $\sigma_{\mathrm{bg}} = \tilde{\sigma} + \hat{\sigma}$. This nonlocal correction to the stress field is non-zero for all surface step heights, even for atomic spacing height. However, for atomic distance sized features any continuum approach looses its validity. This restriction is intrinsically taken into account in this framework as the stress intensity factor K_k decreases to zero as the step height approaches zero.

2.4 Cohesive surface

To model cleavage fracture as the initiation of a fatigue crack, the cohesive surface model of Xu and Needleman (1994) is adopted with properties that approach atomic separation (cf. Cleveringa et al. 2000). This cohesive law couples normal and tangential separation through the expression for the cohesive energy

$$\Phi = \Phi_n - \Phi_n \exp\left(-\frac{\Delta_n}{\delta_n}\right)\left[\left(1 - r + \frac{\Delta_n}{\delta_n}\right)\frac{1-q}{r-1} - \left(q + \frac{r-q}{r-1}\frac{\Delta_n}{\delta_n}\right)\exp\left(-\frac{\Delta_t^2}{\delta_t^2}\right)\right] \tag{5}$$

where Δ_n denotes the normal separation and Δ_t the tangential separation. The corresponding normal and tangential components T_n and T_t of the traction vector $\boldsymbol{T}$ are given by

$$T_n = -\frac{\partial \Phi}{\partial \Delta_n}, \quad T_t = -\frac{\partial \Phi}{\partial \Delta_t}. \tag{6}$$

The work of normal and of tangential separation are denoted by $\Phi_n = \exp(1)\sigma_{\max}\delta_n$ and $\Phi_t = \sqrt{\exp(1)/2}\,\tau_{\max}\delta_t$, respectively, while $\sigma_{\max}$ and $\tau_{\max}$ are the normal and tangential strengths, respectively, and the characteristic lengths are δ_n and δ_t.

The material parameters q and r govern the coupling between the normal and tangential response as

$$q = \frac{\Phi_t}{\Phi_n}, \quad r = \frac{\Delta_n^*}{\delta_n}$$

where Δ_n^* is the value of Δ_n after complete shear separation with $T_n \to 0$ (see Fig. 4a). Abdul-Baqi and Van der Giessen (2001) have investigated the influence of q and r on the cohesive response and have found that for some combinations, the coupled response becomes physically unlikely; $r = q$ gives a physically meaningful response and is what we adopt here. The traction–separation responses in tension and under shear are shown in Fig. 4.

2.5 Boundary value problem

As mentioned before, the nonlinear cohesive law (5) and (6) requires that the $(\hat{\ })$ solution of subproblem (d) in Fig. 1 is obtained in an incremental manner. We also recall that the $(\hat{\ })$ fields have to correct the $(\tilde{\ })$ and $(\bar{\ })$ fields for the boundary conditions. For convenience, we introduce the $(\check{\ })$ fields which are defined as

$$(\check{\ }) = (\tilde{\ }) + (\bar{\ }),$$

so that $(\ ) = (\hat{\ }) + (\check{\ })$.

The virtual work for a body with a cohesive surface, neglecting body forces and surface tension, can be written as

$$\int_V \boldsymbol{\sigma}\,\delta\boldsymbol{\varepsilon}\,dV - \int_{S_{\mathrm{coh}}} \boldsymbol{T}\,\delta\boldsymbol{\Delta}\,dS = \int_{S_{\mathrm{ext}}} \boldsymbol{T}\,\delta\boldsymbol{u}\,dS. \tag{7}$$

with $\boldsymbol{T} = \boldsymbol{\sigma}\boldsymbol{n}$ being the traction vector on the surface with unit outward normal $\boldsymbol{n}$. Here, V is the volume of

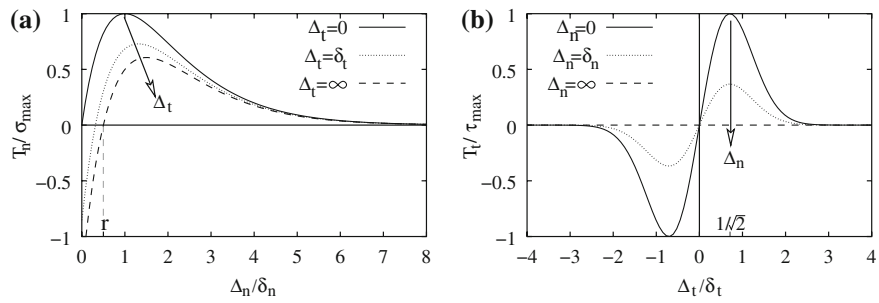

Fig. 4 Coupled traction–separation responses for (**a**) normal and (**b**) tangential direction normalized by the respective strengths σ_{max} and τ_{max}. The open arrows indicate the effect of the cross-coupling on the response

the body analyzed. S_{coh} and S_{ext} are the cohesive and external surface (Fig. 1), respectively. The boundary conditions on S_{ext} are prescribed in terms of prescribed displacements, $\delta\boldsymbol{u} = 0$, or zero tractions $\boldsymbol{T} = 0$. Therefore, the last term in (7) vanishes. As mentioned above, we neglect changes of geometry in order to avoid the complexities of a full finite strain formulation of discrete dislocation plasticity (cf. Deshpande et al. 2003). Yet the separation vector $\boldsymbol{\Delta}$, evidently, contains information about the deformed configuration.

Beside Eq. (7) at time t, we also consider virtual work at $t + \Delta t$. In view of the fact that the $(\tilde{})$ and $(\bar{})$ parts of the decomposition (1) are self-equilibrating, virtual work at $t + \Delta t$ can be simplified to

$$\int_V \hat{\boldsymbol{\sigma}}^{(t+\Delta t)} \delta\boldsymbol{\varepsilon}\, dV - \int_{S_{coh}} \boldsymbol{T}^{(t+\Delta t)} \delta\boldsymbol{\Delta}\, dS = 0. \tag{8}$$

The term that requires due attention is the virtual work done along the cohesive surface.

Cleveringa et al. (2000) were the first to use cohesive surfaces in conjunction with dislocation plasticity and proposed to adopt this Taylor expansion for the cohesive tractions about $t + \Delta t$:

$$\begin{aligned}\boldsymbol{T}\left(\boldsymbol{\Delta}^{(t+\Delta t)}\right) &= \boldsymbol{T}\left(\breve{\boldsymbol{\Delta}}^{(t+\Delta t)} + \hat{\boldsymbol{\Delta}}^{(t+\Delta t)}\right)\\ &= \boldsymbol{T}\left(\breve{\boldsymbol{\Delta}}^{(t+\Delta t)} + \hat{\boldsymbol{\Delta}}^{(t)} + \Delta t\,\dot{\hat{\boldsymbol{\Delta}}}\right)\\ &\cong \boldsymbol{T}\left(\breve{\boldsymbol{\Delta}}^{(t+\Delta t)} + \hat{\boldsymbol{\Delta}}^{(t)}\right)\\ &\quad + \boldsymbol{K}\left(\breve{\boldsymbol{\Delta}}^{(t+\Delta t)} + \hat{\boldsymbol{\Delta}}^{(t)}\right)\Delta t\,\dot{\hat{\boldsymbol{\Delta}}}\end{aligned} \tag{9}$$

where the superposed dot denotes differentiation with respect to time t. Here, $\boldsymbol{K}$ is the instantaneous cohesive stiffness defined by

$$\boldsymbol{K} = \frac{\partial \boldsymbol{T}}{\partial \boldsymbol{\Delta}}$$

We substitute Eq. (9) into (8) along with a first order expansion for the stresses at $t + \Delta t$. Subsequently, after using Eq. (7), we obtain

$$\begin{aligned}&\int_V \dot{\hat{\boldsymbol{\sigma}}}^{(t)} \delta\boldsymbol{\varepsilon}\, dV - \int_{S_{coh}} \boldsymbol{K}\left(\breve{\boldsymbol{\Delta}}^{(t+\Delta t)} + \hat{\boldsymbol{\Delta}}^{(t)}\right) \dot{\hat{\boldsymbol{\Delta}}}\, \delta\boldsymbol{\Delta}\, dS\\ &= \frac{1}{\Delta t}\Big[\int_{S_{coh}} \Big[\boldsymbol{T}\left(\breve{\boldsymbol{\Delta}}^{(t+\Delta t)} + \hat{\boldsymbol{\Delta}}^{(t)}\right)\\ &\quad - \boldsymbol{T}\left(\breve{\boldsymbol{\Delta}}^{(t)} + \hat{\boldsymbol{\Delta}}^{(t)}\right)\Big] \delta\boldsymbol{\Delta}\, dS\end{aligned} \tag{10}$$

After introduction of the usual finite element interpolation functions, the first line of Eq. (10) leads to the left-hand side of the linear system of finite element equations $\mathsf{K}\dot{\mathsf{a}} = \dot{\mathsf{f}}$ (with $\dot{\mathsf{a}}$ the vector of $(\hat{})$ nodal displacement rates). The second line in (10) is the change in energy due to the cohesive surface opening, and gives rise to the right-hand side vector $\dot{\mathsf{f}}$.

3 Problem specification

We simulate the response of a $2\,\mu\text{m} \times 2\,\mu\text{m}$ grain at the free surface, which is initially perfectly flat. A value of $B = 10^{-4}$ Pa s for the drag coefficient is adopted while the applied strain rate is 50,000/s (this is an unrealistically high value, chosen merely from the point of view of computing power). The grain is initially dislocation free, and dislocation sources and obstacles are randomly distributed over the slip planes with densities $100/\mu\text{m}^2$ and $140/\mu\text{m}^2$, respectively. The strength of the obstacles is 150 MPa. Two realizations of dislocation sources are studied here; the obstacles are identical in both realizations. The positions of the sources are identical but their strengths are slightly different, though from the same Gaussian distribution having an average value of 50 MPa and a standard deviation of 10 MPa. As demonstrated by Deshpande et al. (2001a), dislocation dynamics is chaotic: small deviations lead to significantly different results in local behaviour. We chose two slightly different distributions to restrict this study not to a specific distribution and, therefore, specific result. The question is if small differences in

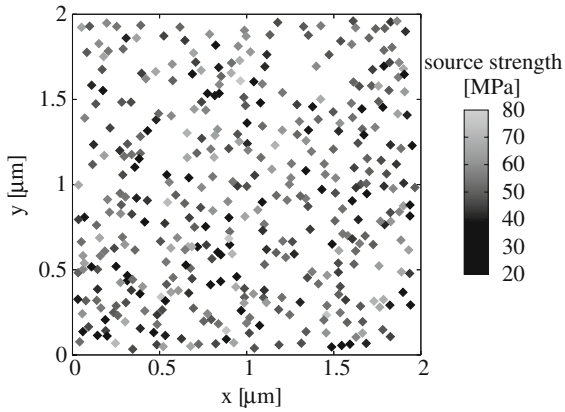

Fig. 5 One of the two realizations of random dislocation sources in a $2 \times 2\,\mu$m grain. The second realization analyzed has the same dislocation positions, but a different selection from the same Gaussian distribution of source strengths

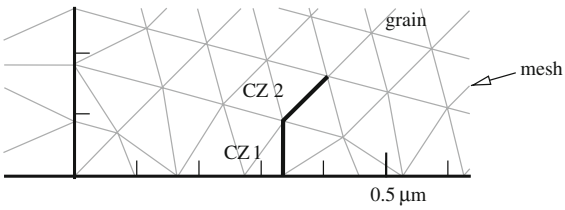

Fig. 6 Lower left-hand corner of a $2 \times 2\,\mu$m grain with two cohesive surfaces

the local properties lead to a significant change in the global response (Fig. 5).

In mere dislocation dynamics simulations, i.e. without cohesive surfaces and surface roughness, of a similar crystal we have observed that the highest in-plane stress σ_{11} at the surface tends to occur between $x = 0$ and $x = 0.7\,\mu$m. The long primary slip planes with the highest dislocation activity, that intersect the free surface roughly within $0 < x < 0.7\,\mu$m, are the reason for the high stress at this location. One of the dislocations in the pair produced by a source tends to move out of the crystal through this section, the sister dislocation remains inside. While dislocation motion relaxes stresses, on average, the long-range interaction of the internally stored dislocations tends to produce a stress field with a high stress at the end of the slip plane, as shown in Brinckmann and Van der Giessen (2004). Another reason for focusing on this area is that the surface roughness is highest here because of the high dislocation activity on the long primary slip planes.

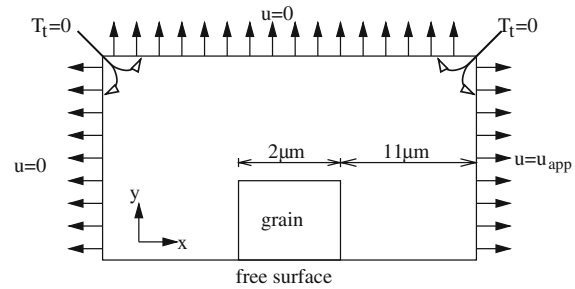

Fig. 7 Boundary conditions and total computational model

Based on these findings, we hypothesize that crack initiation will take place in $0 < x < 0.7\,\mu$m and employ two cohesive elements near the center of this area, as shown in Fig. 6. The first cohesive surface element is normal to the free surface, because the normal stress in the element is maximum in this configuration. The second cohesive element is taken to follow the primary slip system, i.e. 45° to the free surface.

The Poisson ratio $\nu = 0.33$ and the shear modulus is taken to be $\mu = 26\,$GPa. For the cohesive surface we use the same material parameters as have been used previously to model fatigue crack propagation (Deshpande et al. 2002): $r = q = 0.5$ and $\delta_n = \delta_t = 2b = 0.5\,$nm. The cohesive strength is $\sigma_{\max} = 600\,$MPa.

Plastic shearing along a slip system produces dislocation motion. However, it does not damage the material, i.e. it does not reduce the normal strength of the cohesive surface. Therefore, if a cohesive element is parallel to a slip system, e.g. the second cohesive element in Fig. 6, we do not allow for any tangential opening, i.e. $\Delta_t = 0$, so that the normal cohesive properties remain unchanged. For the cohesive element that is normal to the free surface, the normal and tangential modes do interact in such a way that normal opening reduces the tangential strength, and conversely.

Finally, the tangential components of the traction on the boundary are prescribed as zero everywhere. Symmetry, $u_y = 0$, is invoked along the the upper boundary of the computational model, Fig. 7. The remotely applied displacement u_{app}, parallel to the free surface, is taken to vary with time in a zig–zag fashion with $u_{\min} = -u_{\max}$. The maximum displacement is chosen such that it leads to a stress in the grain that is a quarter of the cohesive surface strength when dislocations are not included. Hence, crack initiation is only possible as a consequence of plastic deformation, as is characteristic for fatigue.

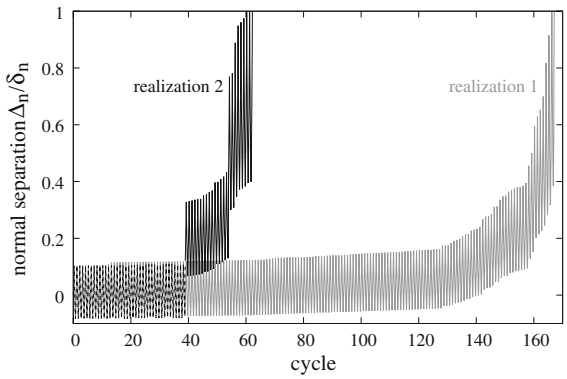

Fig. 8 The normal opening of the first cohesive element Δ_n at the free surface (see Fig. 6) for two realizations of dislocation sources

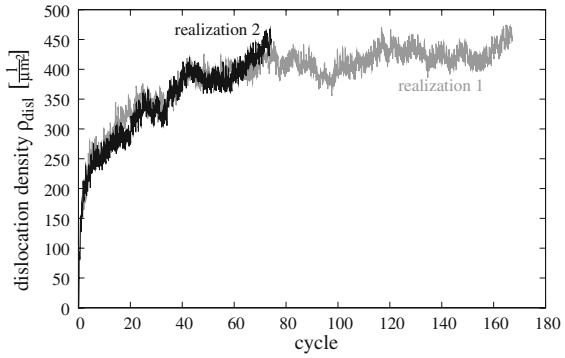

Fig. 9 Dislocation density, corresponding to Fig. 8, in the $2\,\mu$m $\times\, 2\,\mu$m grain for two realizations of dislocation sources

4 Results and Discussion

In Fig. 8 the normal opening of the first cohesive element at the free surface is shown as a function of time. For the first realization of dislocation sources the opening increases slowly for roughly 120 cycles, after which it exhibits a growth rate which increases in every cycle. During the 166th cycle, the opening reaches the critical opening, i.e. $\Delta_n/\delta_n = 1$. We refer to this event as 'fatigue crack initiation' and terminate the simulation at this point. Continuation of the simulation beyond this point would require additional constitutive rules for dislocations wanting to leave the crystal through the cohesive surface, which are not known yet.

The opening response found with the second realization of source strengths is initially similar to that for the first realization, but then features two 'jumps'. After 38.7 cycles the opening increases rapidly. After this jump the rate of increase in opening per cycle is initially the same as before the jump, but gradually increases until the second rapid increase at 53.9 cycles. From this moment on the opening increases even more rapidly and reaches the critical value shortly afterwards. Note that both jumps start during the compressive loading phase and are finished during the subsequent tensile phase.

We now look into the events which led to the first rapid increase, which is the origin for the premature failure. Prior to the jump, dislocations move chaotically back and forth in the changing energy valleys of the potential caused by the other dislocations and the boundary conditions. At almost maximum compressive loading the 'jump' occurs. The duration of this rapid increase is roughly 8,000 time increments and therefore not a single event caused by a numerical instability but a stochastic event. During compression a significant amount of strain energy is stored in the crack process zone. Therefore, it is energetically favorable for dislocations to change to a neighboring valley of the potential, thereby changing the global landscape of the potential and decreasing the closure in the crack process zone. This rapid increase in material separation is what we observe as a jump. The cohesive law (5) induces an exponential traction–separation curve, which leads to the absolute stresses being lower during the tensile phase than during compression. This difference leads to a significantly lower stored strain energy during the tensile phase, which makes reversal of the jump events during the subsequent tensile phase highly unlikely.

The 'jumps' in the opening of the cohesive surface are a local event and do not have a strong effect on the overall response, as is demonstrated in Fig. 9 for the evolution of the overall dislocation density. The dislocation density increases rapidly initially, but the average growth rate decreases in later cycles and approaches a slow but steady average growth rate. However, during a few tens of cycles just prior to fracture initiation, an increase in the dislocation density is observed for both realizations.

Figure 10 shows the deformation in the grain for the first realization of dislocation sources after 164 cycles, i.e. a few cycles before crack initiation. From the misalignment in the mesh lines we can see a rather well-defined shear band aligned with the 45° primary slip direction, just left of the cohesive elements. Where this

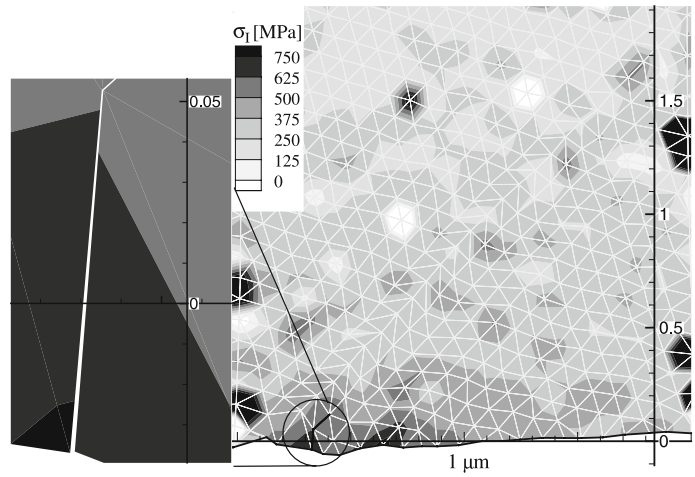

Fig. 10 Distribution of the maximum principal tensile stress superposed on the deformation (magnified by a factor 5) for the first realization of dislocation sources after 164 cycles

band intersects the surface, it has produced a significant intrusion, i.e. a crystallographic surface step into the material. Near this intrusion the principal stresses are on average 250 MPa higher than in the remainder of the grain. These high tensile stresses lead to the initiation of the fatigue crack.

It bears emphasis that in the first cohesive element, the tangential opening is smaller than the normal opening. Therefore, this framework predicts that fatigue initiation is associated with mode I crack opening. Furthermore, the crack opening is maximum at the free surface, i.e. the crack initiates at the free surface and grows into the grain.

As in the fatigue crack growth simulations in Deshpande et al. (2001b, 2002), the strength of the cohesive surface, $\sigma_{\max} = 600\,\text{MPa}$, is not reflecting actual atomic bond properties even though the normal fracture energy $\Phi_n = 0.82\,\text{J/m}^2$ is realistic. The cohesive strength has been chosen smaller than atomic properties in order for the computation to finish in an accessible time. Therefore, together with our high applied strain rate, the number of cycles to reach fatigue crack initiation is much smaller than those found in experiments. With a higher cohesive strength the material is expected to break later assuming continued growth in the local dislocation-induced normal traction.

In the computations presented above, the evolution of surface roughness and dislocation plasticity interacted in an intricate manner through their stress fields. To study whether surface roughness is a necessary contribution for fatigue crack initiation, one simulation (using the first realization of sources) is repeated but without taking surface roughness into account (i.e. the ($\bar{}$) fields are ignored). Figure 11 shows the effect of the presence of surface roughening on the evolution of the fatigue crack and dislocation density. While Fig. 8 revealed crack initiation within the first 167 cycles, the computation without including surface roughening does not lead to any appreciable accumulation of the normal opening at the free surface over the same period. Therefore, the surface roughness is a significant contribution to fatigue crack initiation. This seems to be supported by the experimental finding by Hahn and Duquette (1978) that repeated removal of the surface roughness leads to a significant delay in fatigue crack initiation. Moreover, the present study shows that fatigue crack initiation in the material interior is less likely than cracks at the surface because interior cracks lack the contribution from surface roughness.

The evolution of dislocation density, shown in Fig. 11b, appears not to depend on the surface roughness. Thus, the dislocation density depends on the initial conditions (dislocation source and obstacle distribution, grain geometry) and on the applied loading (history). The dislocations that glide to the surface and produce surface roughness, have virtually no effect on the dislocation density evolution, but this surface roughness is necessary for the initiation of a fatigue crack.

5 Concluding remarks

We have proposed a new computational framework that combines discrete dislocation plasticity and cohesive surfaces with a surface roughness model. While

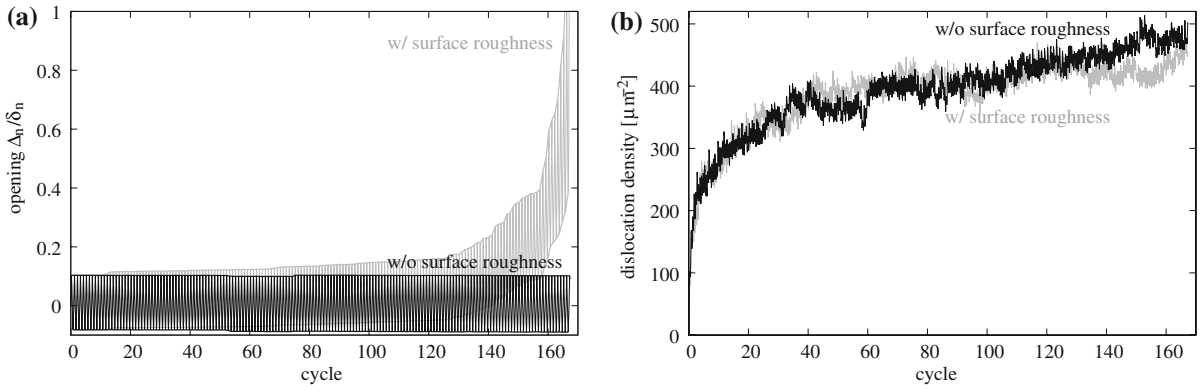

Fig. 11 Evolution of the normal opening of the first cohesive element Δ_n at the free surface (**a**) and the evolution of the dislocation density (**b**) for a simulation including the surface roughness and one excluding it

the first two ingredients were already present in the studies of fatigue crack growth by Deshpande et al. (2001b, 2002), the extension with a description of surface roughening is necessary for fatigue initiation.

It bears emphasis that damage evolution in this approach is not assumed, but an outcome of the simulation. Damage, in this framework, can be viewed as the gradual evolution of the dislocation distribution and accumulation of surface roughness.

This framework was employed to simulate the behavior of a favorably oriented grain at the free surface under remote tension–compression cycles. Fatigue crack initiation at the free surface is predicted as the cooperative effect of the build-up of local stress by evolution of the dislocation distribution and development of surface roughness. We here recall the observation in Cleveringa et al. (2000) that dislocations play a dual role in fracture: on the one hand they mediate stress relaxation by plastic flow, but at the same time they lead to local stress levels of the magnitude of the cohesive strength due to discrete dislocations in the vicinity of the crack tip. The opening of a cohesive surface, as a model of atomic separation, in the tensile direction increases slowly in the initial cycles but after a certain number of cycles accelerates till reaching the critical opening. Even though the crack initiates next to a persistent slip band, the sliding displacement along the cohesive surface is small compared to the normal opening, so that we conclude that fatigue initiation is a mode I feature. There are suggestions in the literature (e.g. Suresh 1998), that fatigue initiation contains a significant mode II component, but it should be kept in mind that our calculations only pertain to the very first instant of crack initiation, which is probably not observable experimentally.

Deshpande et al. (2001a) have shown that dislocation dynamics is chaotic: arbitrarily small perturbations of the source positions lead to finitely different dislocation structures. They also showed that the perturbed dislocation structure does not need to lead to a different overall response, as in the case of the tensile response of a crystal, but that the response of crack problems is generally affected significantly since crack growth is controlled by local stress fluctuations. This phenomenon has also been observed in the present study. The two random realizations give rise to crack initiation times that differ by at least a factor of two. A random minor event in one of the realizations triggered a series of events which led to a decrease in closure induced stresses. It should be noted, though, that this variability will not translate into fatigue lifetimes, since this also requires a certain amount of crack growth. Also, there is a much larger ensemble of possible initiation sites in real polycrystalline materials.

The present work is a first step to shed light on fatigue crack initiation employing the present framework. The parameters have been chosen to allow for a 'proof of principle' within achievable computing times (of many months on a multi-processor computer). Restrictions on computing time, unfortunately, did not enable a more systematic study, while the mesh density is already questionable. One of the limitations is the use of size-independent linear elasticity to model the surface steps, whose unit magnitude is that of a Bur-

gers vector. Also, unfortunately, our calculations do not predict dislocation patterning in ladder-like structures as observed experimentally in Mughrabi et al. (1979), but the predicted slip bands are comparable to the slip in persistent slip bands. Ladder-like structures might be predicted by simulations employing the extended constitutive rules of Benzerga et al. (2004), which incorporate three-dimensional physics of dislocation interaction. This extended model therebye holds the promise of being able to predict dislocation patterning, but the effect of that on crack initiation remains to be investigated.

Acknowledgements We gratefully acknowledge the computational resources for the present work, which were provided by the Materials Science Center, University of Groningen, The Netherlands.

6 Appendix: Approximation of elastic fields due to a discrete crystallographic surface step

The elastic solutions for a crystallographic surface step given by Brochard et al. (2000), Marchenko and Parshin (1980) and Kukta and Bhattacharya (2002) are not in agreement with the numerical solution we obtained. In this section, we therefore formulate a novel analytical approximation, making use of wedge theory.

We consider a single crystallographic surface step, shown schematically in Fig. 12. The elastic fields at each point scale linearly with the stress σ_{bg} applied parallel to the free surface. The surface steps considered here are produced by dislocations that have left the crystal. Since the crystal has three slip systems, there are six possible wedge angles (two for each slip system, depending on the sign of the dislocations having moved out).

To investigate the dependence of the stress field on the surface step opening angle $2(\pi - \alpha)$, a series of numerical calculations is executed. The effect of the additional stress to the uniform background stress, i.e. the singular stress due to the surface step, is shown in Fig. 13 for some point P in the proximity of the wedge tip. When $\alpha \to \pi/2$, i.e. the flat surface, the singular stress approaches zero. When $\alpha \to \pi$, i.e. an

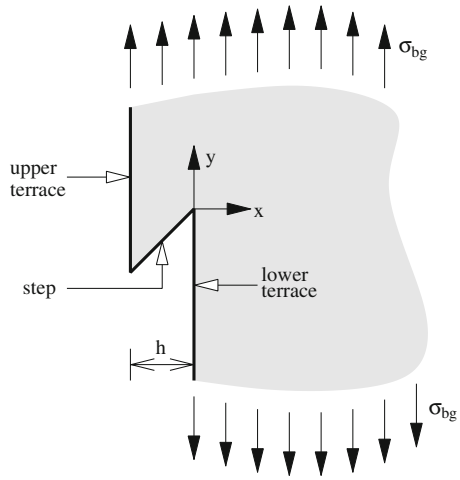

Fig. 12 Definitions used for the surface step

infinitely sharp wedge, these stresses increase significantly. Between the extreme configurations, the stresses can be considered independent of α. Since the most important of the six surface steps relevant here lie inside the constant region, the stress arising from the surface step is considered independent of the wedge angle.

An opening angle of 45° is employed as being representative. For this case, Fig. 14 shows the distribution of the normal stresses in the $6\,\mu\text{m} \times 6\,\mu\text{m}$ around the step. This step has a height $h = 1\,\mu\text{m}$ and is embedded in a $200\,\mu\text{m} \times 200\,\mu\text{m}$ block of isotropic material.

We proceed by approximating this field by means of the asymptotic elastic plane strain field of a wedge in infinite space (Timoshenko and Goodier 1961), as illustrated in Fig. 15a. This means that the traction-free sides of the step itself are accounted for, but the traction-free surface is not. The stresses should thus not be expected to be accurate at distances h away from the internal cusp of the step, but this will be checked later on. The definitions of the local coordinate systems and angles for an infinitely long wedge with an opening angle of $2(\pi - \alpha)$ are shown in Fig. 15b.

We use the asymptotic solution for a wedge given by Timoshenko and Goodier (1961). The associated stress field is a power expansion of the type $r^{\lambda-1}$ with the λ's, distinguished here by the subscript k, being the solution of $(\lambda \sin 2\alpha)^2 = (\sin 2\alpha\lambda)^2$ with α the wedge angle. Dimensional analysis of r and normalization by the background stress σ_{bg} (cf. Fig. 12) then leads to the following expression for the stress field:

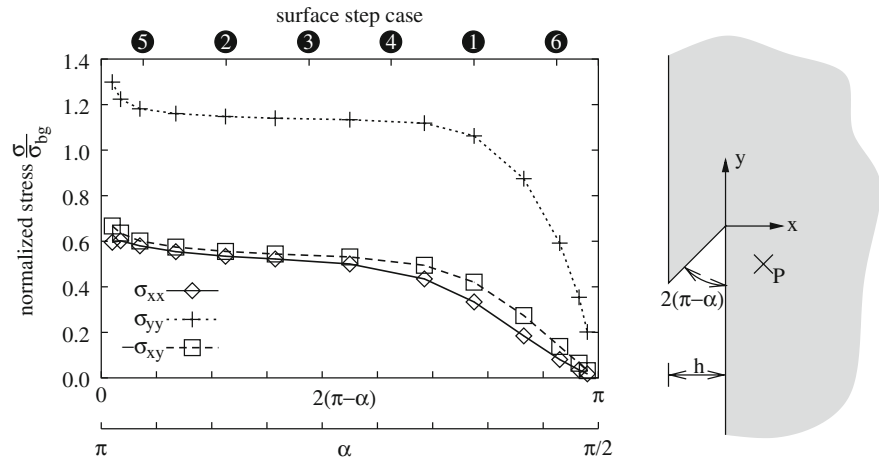

Fig. 13 Numerical calculation: perturbation stresses relative to the uniform background tensile stress σ_{bg} in the y-direction at point $P = (3/5h, -3/5h)$ (chosen arbitrarily) caused by surface step for different step angles

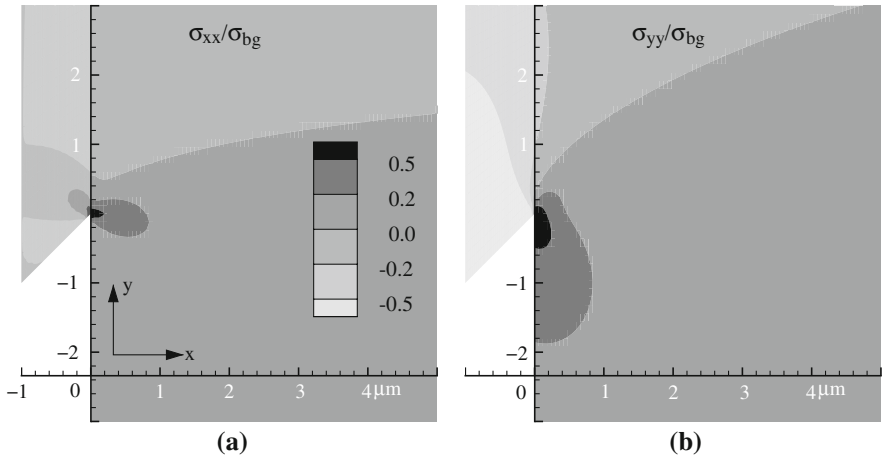

Fig. 14 Normal stress components σ_{xx} (**a**) and σ_{yy} (**b**) for a representative surface step in a $200 \times 200\,\mu$m block subjected to a remote stress $\sigma_{yy} = \sigma_{bg}$ according to finite element calculation

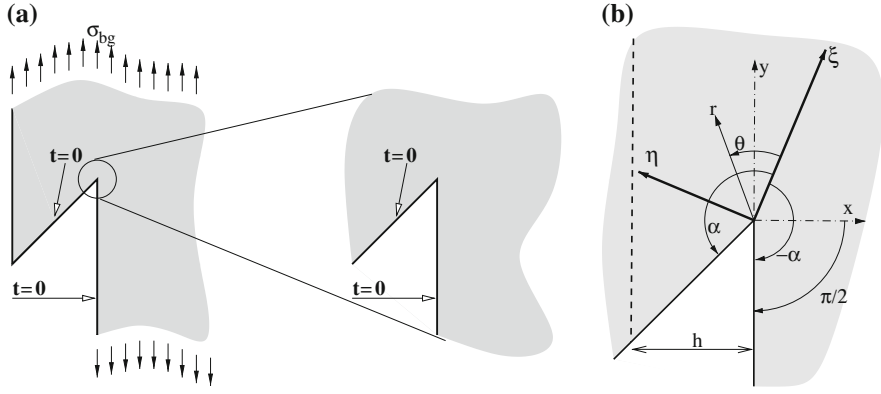

Fig. 15 (**a**) Approximation of the elastic fields due to a surface step. (**b**) Definitions used for the solution of an infinitely long wedge

$$\boldsymbol{\sigma} = \sum_k r^{\lambda_k - 1} K_k \boldsymbol{f}_k^*(\lambda_k, \theta), \qquad K_k = a_k \sigma_{bg} h^{1-\lambda_k},$$
$$\boldsymbol{f}_k^* = \frac{\boldsymbol{f}_k}{\sqrt{f_{xx}^2 + 2f_{xy}^2 + f_{yy}^2}}. \tag{11}$$

For the representative surface step, i.e. $2(\pi - \alpha) = \pi/4$ or $\alpha = 7/8\pi$, two values of λ_k can be determined from $(\lambda \sin 2\alpha)^2 = (\sin 2\alpha\lambda)^2$ (Timoshenko and Goodier 1961), for each of which the vector $\boldsymbol{f}_k^*$ is calculated. This leaves the coefficients a_k of Eq. (11) as unknown parameters, which we establish by fitting the

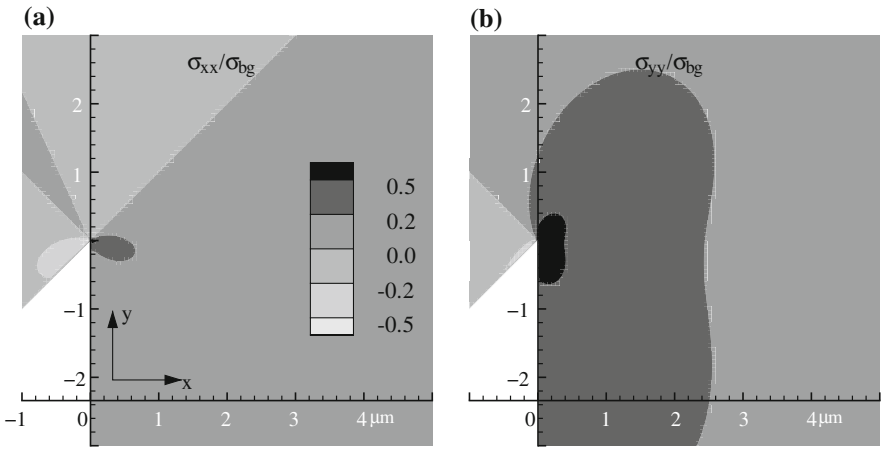

Fig. 16 Approximate stress distribution near a surface step using the wedge solution. Stress components in the x-direction (**a**) and in the y-direction (**b**)

resulting stress fields to the numerical results (Fig. 14). Figure 16 gives the resulting distribution of σ_{xx} and σ_{yy}. Comparison with Fig. 14 reveals that there are points of agreement and disagreement. The stress component σ_{xx} is matched quite well, except at points close to the upper terrace (see Fig. 12). These points have a negative x-coordinate and, therefore, lie outside the region of analysis for the small-strain formulation of the dislocation dynamics model. Therefore, the error in this region is not significant. The stress component in the y-direction is overestimated by the approximation.

The differences between the approximate analytical and the numerical solution arise because the traction-free conditions along the upper surface terrace (see Fig. 12) are not taken into account by this asymptotic approach (cf. also dashed line in Fig. 15b). Only the boundary conditions on the lower terrace and the step are accounted for. The influence of the boundary conditions along the upper surface terrace is strong in the area shown in Fig. 16 because the surface step height is on the same order of length as the size of the area of interest. Nevertheless, since this approximation yields better agreement than any of the other solutions in the literature mentioned in the beginning of this appendix, we employ it in the present study.

References

Abdul-Baqi A, Van der Giessen E (2001) Delamination of a strong film from a ductile substrate during indentation unloading. J Mater Res 16:1396–1407

Antonopoulos JG, Brown LM, Winter AT (1976) Vacancy dipoles in fatigued copper. Philos Mag 34:549–563

Basinski ZS, Basinski SJ (1985) Low amplitude fatigue of copper single crystals – II. Surface observations. Acta Metall 33:1307–1317

Benzerga AA, Bréchet Y, Needleman A, Van der Giessen E (2004) Incorporating three-dimensional mechanisms into two-dimensional dislocation dynamics. Model Simul Mater Sci Eng 12:159–196

Brinckmann S, Van der Giessen E (2004) A discrete dislocation dynamics study aiming at understanding fatigue crack initiation. Mater Sci Eng A 387–389:461–464

Brochard S, Beauchamp P, Grilhé J (2000) Stress concentration near a surface step and shear localization. Phys Rev B 61:8707–8713

Brown LM, Ogin SL (1984) Role of internal stresses in the nucleation of fatigue cracks. In: Willis JR, Bilby BA, Miller KJ (eds) Fundamentals of deformation and fracture. Eshelby memorial symposium, pp 501–528

Cleveringa HHM, Van der Giessen E, Needleman A (2000) A discrete dislocation analysis of mode I crack growth. J Mech Phys Solids 48:1133–1157

Déprés C, Robertson CF, Fivel MC (2004) Crack initiation in fatigue: experiments and three-dimensional dislocation simulations. Mater Sci Eng A 387–389:288–291

Deshpande VS, Bréchet Y, Needleman A, Van der Giessen E (2001a) Dislocation dynamics is chaotic. Scripta Mater 45:1047–1053

Deshpande VS, Needleman A, Van der Giessen E (2001b) A discrete dislocation analysis of near-threshold fatigue crack growth. Acta Mater 49:3189–3203

Deshpande VS, Needleman A, Van der Giessen E (2002) Discrete dislocation modelling of fatigue crack propagation. Acta Mater 50:831–846

Deshpande VS, Needleman A, Van der Giessen E (2003) Finite strain discrete dislocation plasticity. J Mech Phys Solids 51:2057–2083

Essmann U, Gösele U, Mughrabi H (1981) A model of extrusions and intrusions in fatigued metals – I. Point-defect production and the growth of extrusions. Philos Mag A 44:405–426

Fine ME, Bhat SP (2007) A model of fatigue crack nucleation in single crystal iron and copper. Mater Sci Eng A 468–470:64–69

Freund LB (1994) The mechanics of dislocations in strained-layer semiconductor materials. Adv Appl Mech 30:1–66

Hahn HN, Duquette DJ (1978) The effect of surface dissolution on fatigue deformation and crack nucleation in copper and copper 8% aluminum single crystals. Acta Metall 26: 279–287

Hirth JP, Lothe J (1968) Theory of dislocations. McGraw-Hill, New York

Kratochvil J (2001) Self-organization model of localization of cyclic strain into PSBs and the formation of dislocation wall structures. Mater Sci Eng A 309–310:331–335

Kukta RV, Bhattacharya K (2002) A micromechanical model of surface steps. J Mech Phys Solids 50:615–649

Marchenko VI, Parshin AY (1980) Elastic properties of crystal surfaces. Sov Phys JETP 52:129–131

Mughrabi H, Ackermann F, Herz K (1979) Persistent slip bands in fatigued face-centered and body-centered cubic metals. In: Fatigue mechanisms, Special Technical Publication 675. American Society for Testing and Materials, Philadelphia, pp 69–105

Narasaiah N, Ray KK (2008) Initiation and growth of mirco-cracks under cyclic loading. Mater Sci Eng A 474(1–2):48–59

Neumann P (1969) Coarse slip model of fatigue. Acta Metall 17:1219–1225

Polák J (2007) Mechanisms and kinetics of the early fatigue damage in crystalline materials. Mater Sci Eng A 468–470:33–39

Repetto EA, Ortiz M (1997) A micromechanical model of cyclic deformation and fatigue-crack nucleation on f.c.c. single crystals. Acta Mater 45:2577–2595

Sackett EE, Germain L, Bache MR (2007) Crystal plasticity, fatigue crack initiantion and fatigue performante of advanced titanium alloys. Int J Fatigue 29:2015–2021

Suresh S (1998) Fatigue of materials. 2. Cambridge University Press, Cambridge, UK

Timoshenko S, Goodier JN (1961) Theory of elasticity. 2. McGraw-Hill, New York

Van der Giessen E, Needleman A (1995) Discrete dislocation plasticity: a simple planar model. Model Simul Mater Sci Eng 3:689–735

Vehoff H (1994) Rissbildung und Rissausbreitung in Ein- und Bikristallen. VDI Verlag

Xu XP, Needleman A (1994) Numerical simulations of fast crack growth in brittle solids. J Mech Phys Solids 42:1397–1434